Supplement of The Cryosphere, 20, 495–510, 2026
https://doi.org/10.5194/tc-20-495-2026-supplement

The Cryosphere Open Access EGU

Supplement of

Inferring the ice sheet sliding law from seismic observations: A Pine Island Glacier case study

Kevin Hank et al.

Correspondence to: Kevin Hank (kevhan@bas.ac.uk)

S1 Basal ice speed and basal drag map

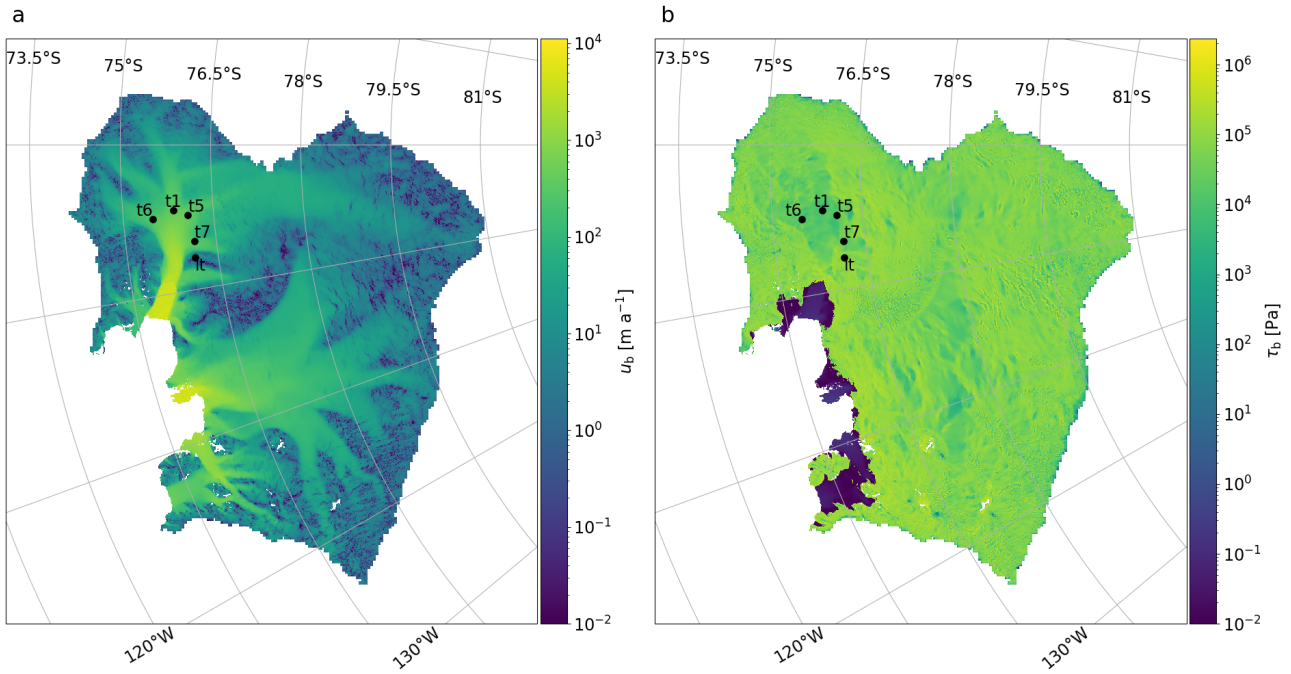

Figure S1. Basal sliding speed (a) and basal drag (b) in the Amundsen Sea Embayment retrieved from the surface-to-bed inversion. The black dots mark the locations of the seismic observation sites.

S2 Posterior probabilities when using sub-sampled data

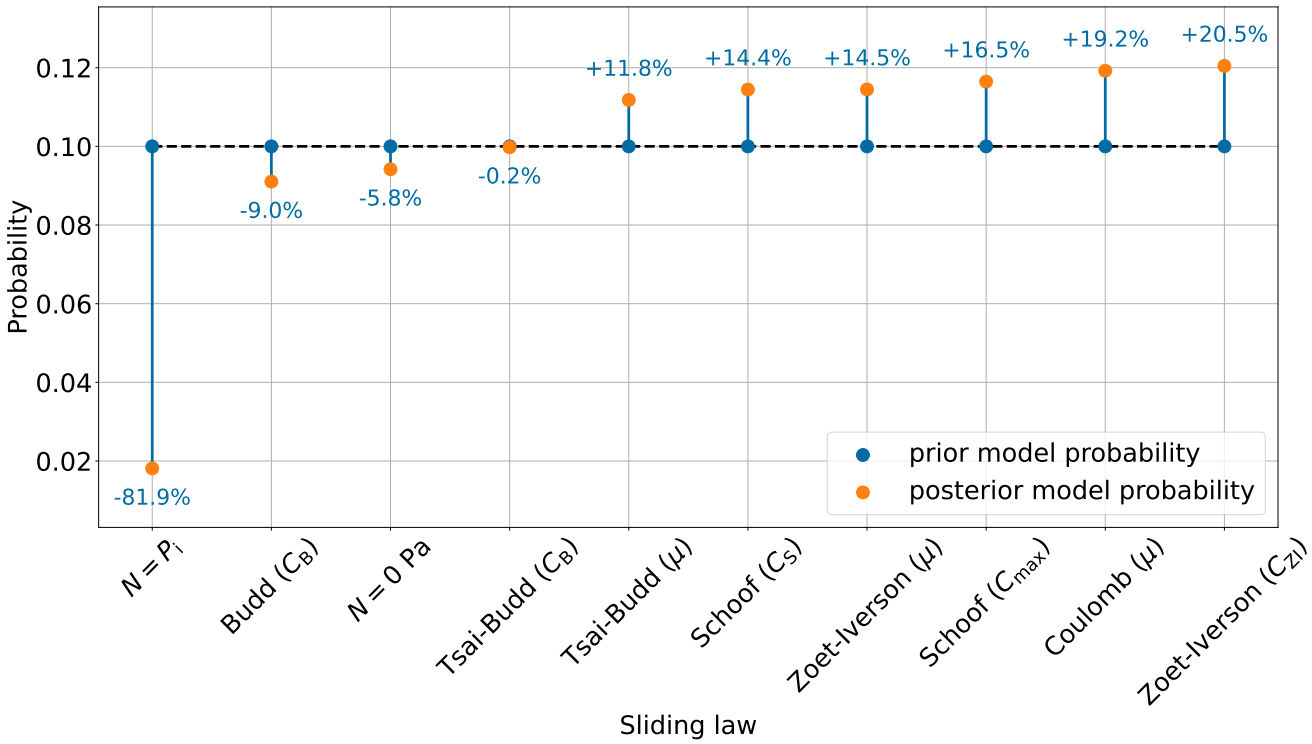

Figure S2. Normalized probabilities (Eq. 20) when using only every 10th acoustic impedance measurement collected on Pine Island Glacier (PIG). Due to the small changes in the posterior model probabilities (Fig. S3) but significant increases in computational cost, we did not run sub-sampled experiments for the 4D sliding laws. Limiting Θ_i to 3D leads to two different representations of the Tsai-Budd, Schoof, and Zoet-Iverson sliding law with one sliding law parameter fixed. The fixed parameters are $\mu = 0.5$ for Tsai-Budd (C_B), $C_\mathrm{B} = 37.01\ \mathrm{m}^{-1/3}\ \mathrm{s}^{1/3}$ (based on minimum misfit when varying C_B) for Tsai-Budd (μ), $C_\mathrm{max} = 0.2$ for Schoof (C_S), $C_\mathrm{S} = 1 \cdot 10^3\ \mathrm{MPa}\ \mathrm{m}^{-1/3}\ \mathrm{s}^{1/3}$ (value closest to $C_\mathrm{S} = 7.624\ \mathrm{MPa}\ \mathrm{m}^{-1/3}\ \mathrm{s}^{1/3}$ suggested by Brondex et al. (2017) while ensuring low percentage of incompatible $u_\mathrm{b}-\tau_\mathrm{b}$ pairs; Sec. S5; Fig S15 and S16) for Schoof (C_max), $\mu = 0.5$ for Zoet-Iverson (C_ZI), and $C_\mathrm{ZI} \sim 340\ \mathrm{MPa}^{-1}\ \mathrm{m\,a}^{-1}$ (as suggested by Zoet and Iverson, 2020) for Zoet-Iverson (μ). Unless indicated otherwise, these values correspond to the highest prior probability. Otherwise, as Fig. 6 in the main text.

S3 3D-4D parameter space comparison

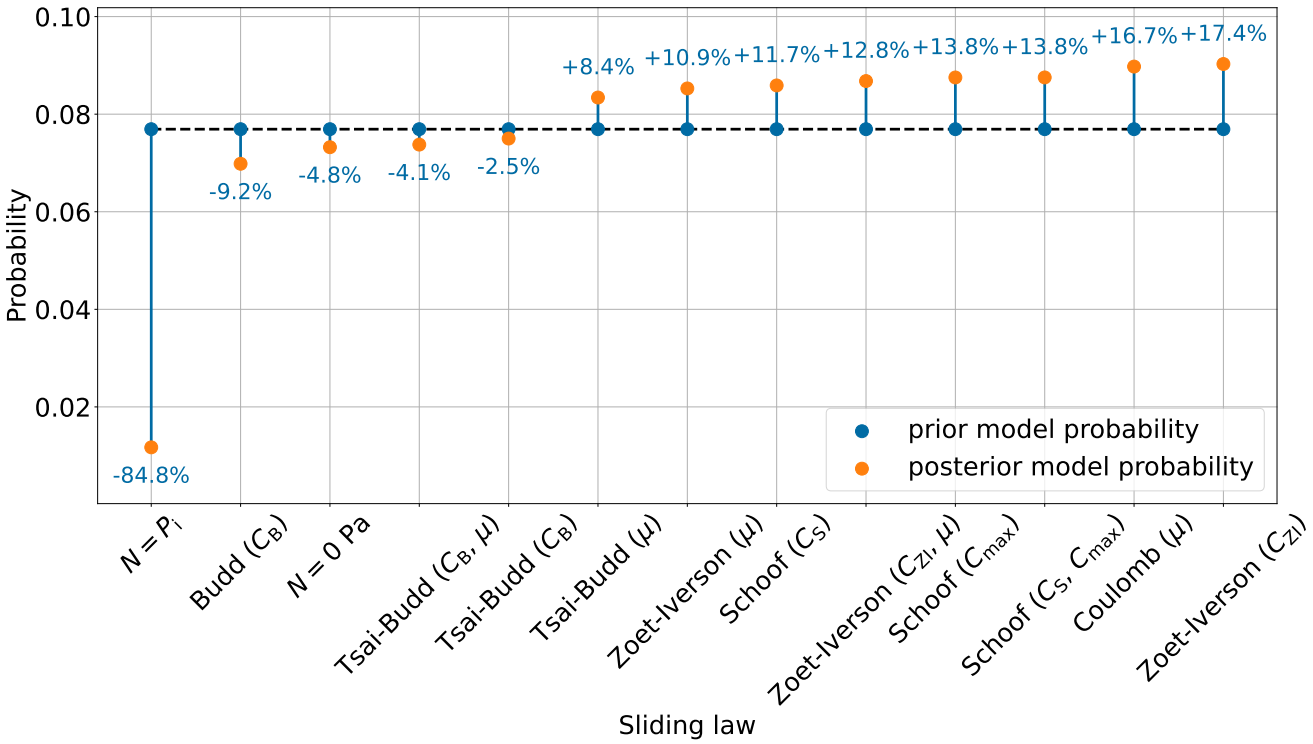

Figure S3. Normalized probabilities (Eq. 20) when limiting the model parameter space Θ_i to 3D compared to the full 4D results. Limiting Θ_i to 3D leads to two different representations of the Tsai-Budd, Schoof, and Zoet-Iverson sliding law with one sliding law parameter fixed. The fixed parameters are $\mu = 0.5$ for Tsai-Budd (C_B), $C_\mathrm{B} = 37.01\ \mathrm{m}^{-1/3}\ \mathrm{s}^{1/3}$ (based on minimum misfit when varying C_B) for Tsai-Budd (μ), $C_\mathrm{max} = 0.2$ for Schoof (C_S), $C_\mathrm{S} = 1 \cdot 10^3\ \mathrm{MPa}\ \mathrm{m}^{-1/3}\ \mathrm{s}^{1/3}$ (value closest to $C_\mathrm{S} = 7.624\ \mathrm{MPa}\ \mathrm{m}^{-1/3}\ \mathrm{s}^{1/3}$ suggested by Brondex et al. (2017) while ensuring low percentage of incompatible $u_\mathrm{b}-\tau_\mathrm{b}$ pairs; Sec. S5; Fig S15 and S16) for Schoof (C_max), $\mu = 0.5$ for Zoet-Iverson (C_ZI), and $C_\mathrm{ZI} \sim 340\ \mathrm{MPa}^{-1}\ \mathrm{m\ a}^{-1}$ (as suggested by Zoet and Iverson, 2020) for Zoet-Iverson (μ). Unless indicated otherwise, these values correspond to the highest prior probability. Otherwise, as Fig. 6 in the main text.

S4 Metrics involved in determining the acoustic impedance misfit

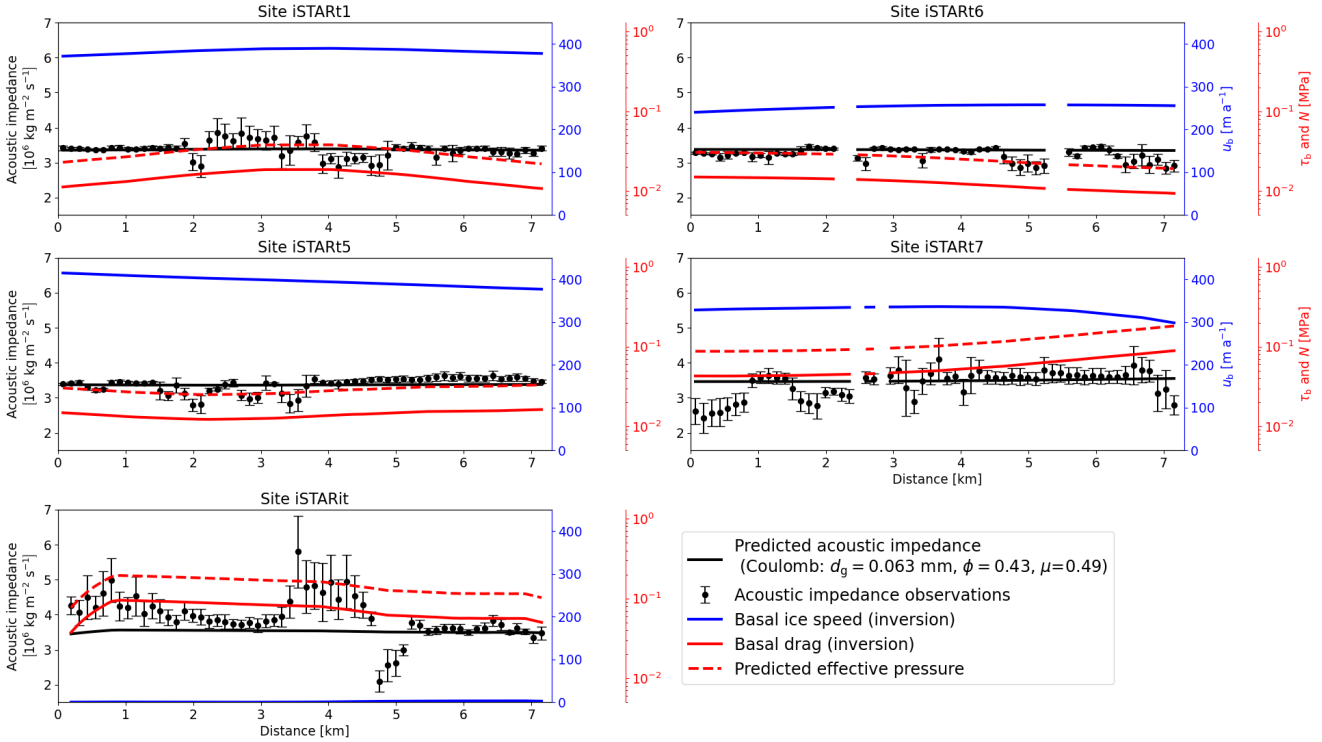

Figure S4. Metrics involved in predicting the acoustic impedance based on the Viscous Grain-Shearing (VGS) theory and calculating the misfit to the seismic observations. The black, blue, and red colours (lines, points, and axes) represent acoustic impedance, basal ice speed, and basal drag and effective pressure, respectively. The results are based on the Coulomb sliding law with the maximum a posteriori (MAP) parameter values.

S5 Incompatible $u_b - \tau_b$ pairs for small C_S values

When using the Schoof sliding law, C_S values smaller than $1 \cdot 10^3$ MPa m$^{-1/3}$ s$^{1/3}$ (e.g., $C_S = 7.624$ MPa m$^{-1/3}$ s$^{1/3}$ suggested by Brondex et al., 2017) show a high percentage of incompatible (can not be explained by Eq. 7) $u_b - \tau_b$ pairs, inhibiting the determination of a misfit (Fig. S5, S15, and S16; see also Brondex et al., 2019). As this information is available prior to applying the Bayesian model selection, but was not used to constrain the C_S prior, we update $P(\Theta_i|M_i)$ by incorporating the information from the inverted $u_b - \tau_b$ using Bayes' rule (Eq. 19). However, the posterior probabilities without this normalization are shown in Fig. S6. Since the chosen parameter space Θ_i does not lead to incompatible $u_b - \tau_b$ pairs near the seismic data sites for any of the other sliding laws, their posterior probabilities are not affected. Note that their final normalized probabilities differ because of the change in the posterior probability of the Schoof sliding law.

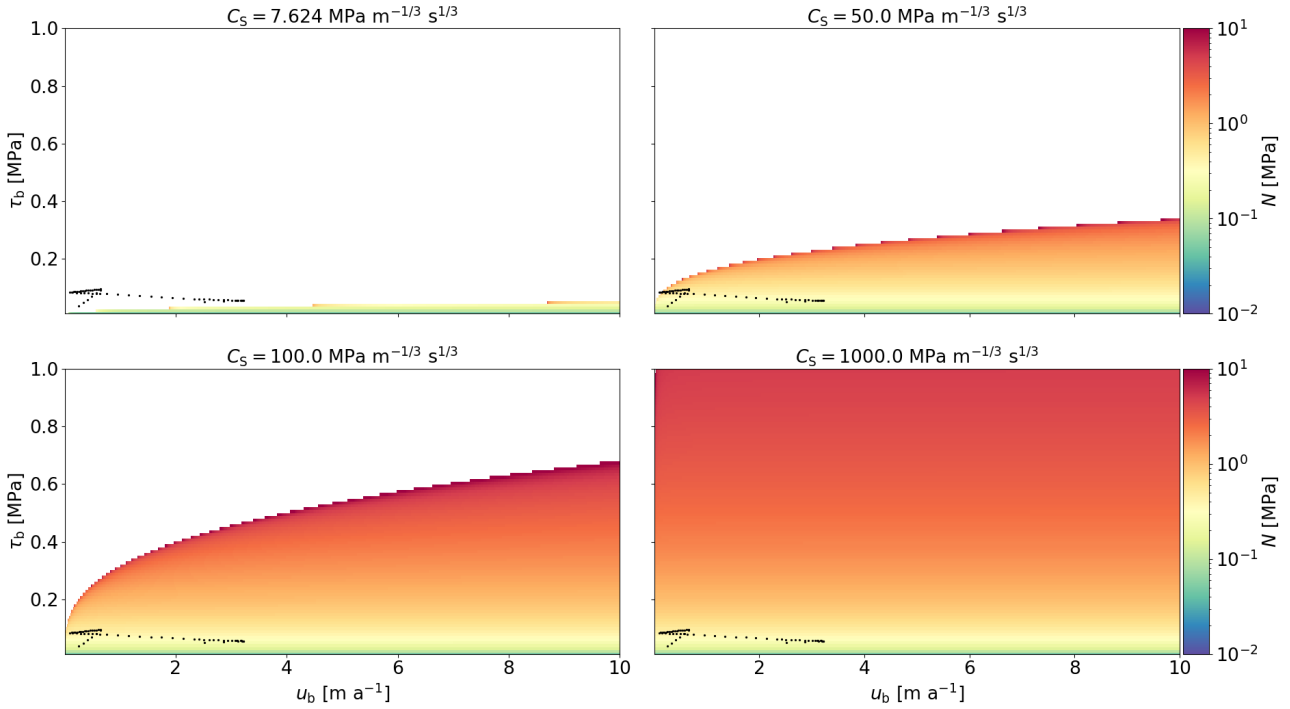

Figure S5. Simple toy experiment illustrating the $u_b - \tau_b$ pairs incompatible with Eq. 7 for different C_S values ($C_{max} = 0.2$ and $m = 1/3$). Smaller C_S values, generally corresponding to smoother beds, lead to more incompatible $u_b - \tau_b$ pairs (larger white area). This issue primarily arises for small u_b and comparatively large τ_b values at site iSTARit located between two tributaries (black dots).

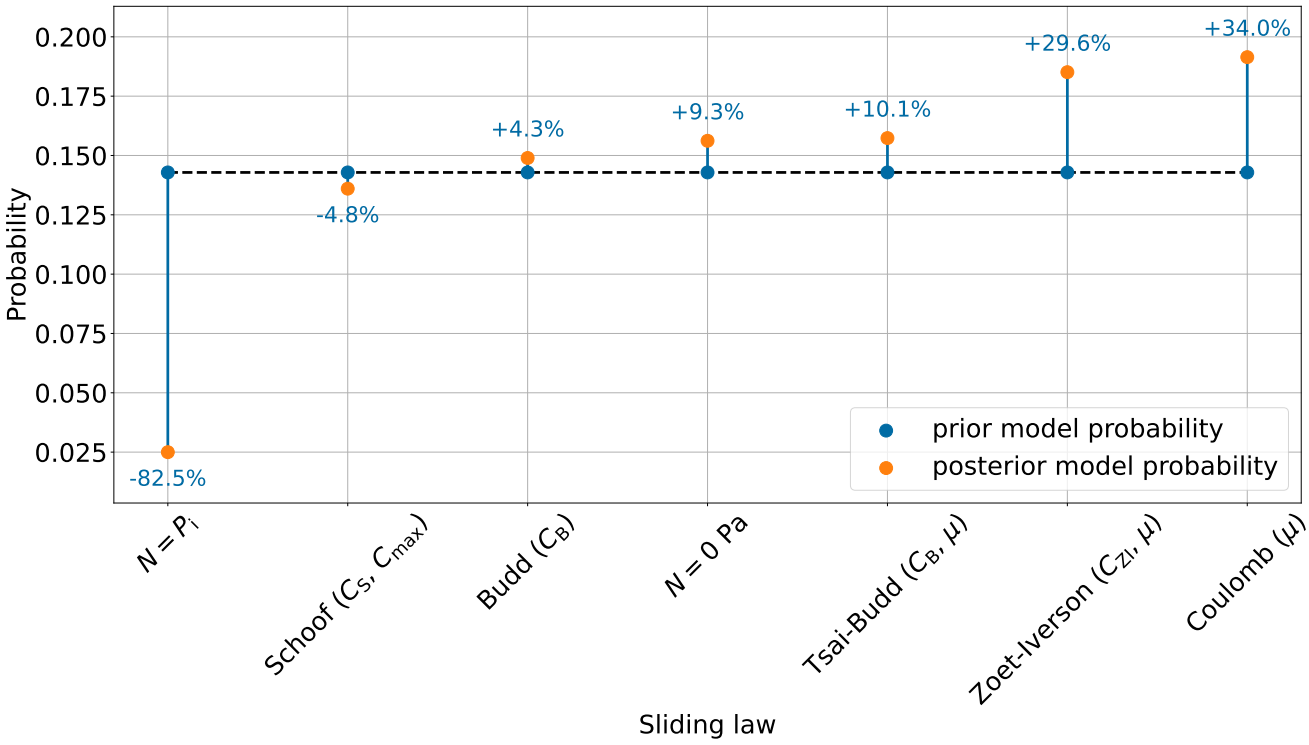

Figure S6. Normalized probabilities (Eq. 18) of all sliding laws examined in this study given the acoustic impedance observations collected on PIG. The prior model probability is taken as $P(M_i) = 1/n$, rather than $P(M_i|I) = 1/n$, and consequently, no normalization via $P(I|M_i)$ (Eq. 19) is applied. This leads to a significant reduction in the posterior probability of the Schoof sliding law due to an increasing number of incompatible $u_\mathrm{b}-\tau_\mathrm{b}$ pairs for C_S values smaller than $1 \cdot 10^3$ MPa $\mathrm{m}^{-1/3}$ $\mathrm{s}^{1/3}$ (see Fig. S5 for a simple toy experiment), resulting in overall 27 % of the likelihood being undefined (NaN), which is treated as zero likelihood here. Otherwise, as Fig. 6 in the main text.

S6 Prior distribution

S6.1 Porosity and grain diameter

Site	Porosity [%]	Clay [%]	Silt [%]	Sand [%]	Gravel [%]	Facies	Notes
BEAMISH	35	8	36	30	27	ST	Recovered from beneath Rutford Ice Stream (Smith, unpublished data)
PIGA	36	30	31	26	13	IT	Recovered from PIG ice shelf (Smith et al., 2017)
PIGB	39	28	28	33	11	IT	Recovered from PIG ice shelf (Smith et al., 2017)
VC415	34	3	46	36	14	ST	Deposited seaward of Dotson Ice Shelf during the Last Glacial Maximum (Smith et al., 2011)
VC417	35	3	51	37	8	ST	Deposited seaward of Dotson Ice Shelf during the Last Glacial Maximum (Smith et al., 2011)

Table S1. Porosity and grain diameter data used to determine the corresponding prior distributions. The facies are ice tranistional sediment deposited at or close to the grounding line (IT) and subglacial till deposited at the base of the ice stream (deformation till; ST).

S6.2 Maximum up-slope angle of the bed and Iken's bound

The distribution of the up-slope angles of the bed in flow direction (β) and the corresponding Iken's bound ($C_{\max} = \tan(\beta)$; Fig. S7) is examined for the center part of Pine Island Glacier (PIG; magenta box in Fig. S8). As the horizontal grid resolution of Bedmap2 is $1\ \mathrm{km}$ (Fretwell et al., 2013), the maximum up-slope angle (and therefore $C_{\max}$) on smaller scales might be significantly steeper than suggested by the distribution in Fig. S7. For example, autonomous underwater vehicle (AUV) data collected downstream of Thwaites Glacier ($1.5\ \mathrm{m}$ horizontal resolution; Graham et al., 2022) and under the Thwaites Eastern Ice Shelf ($2\ \mathrm{m}$ horizontal resolution; Wåhlin et al., 2026) indicate that the maximum $C_{\max} > 0.7$ (largest value tested within this study; Fig. S9). As the bed roughness and therefore the actual relevant scale are unknown and likely vary spatially, the chosen $C_{\max}$ prior incorporates the coarse resolution Bedmap2 data as a conservative lower bound and accounts for the higher bed angles observed at smaller scales through a more gradual decline towards higher values.

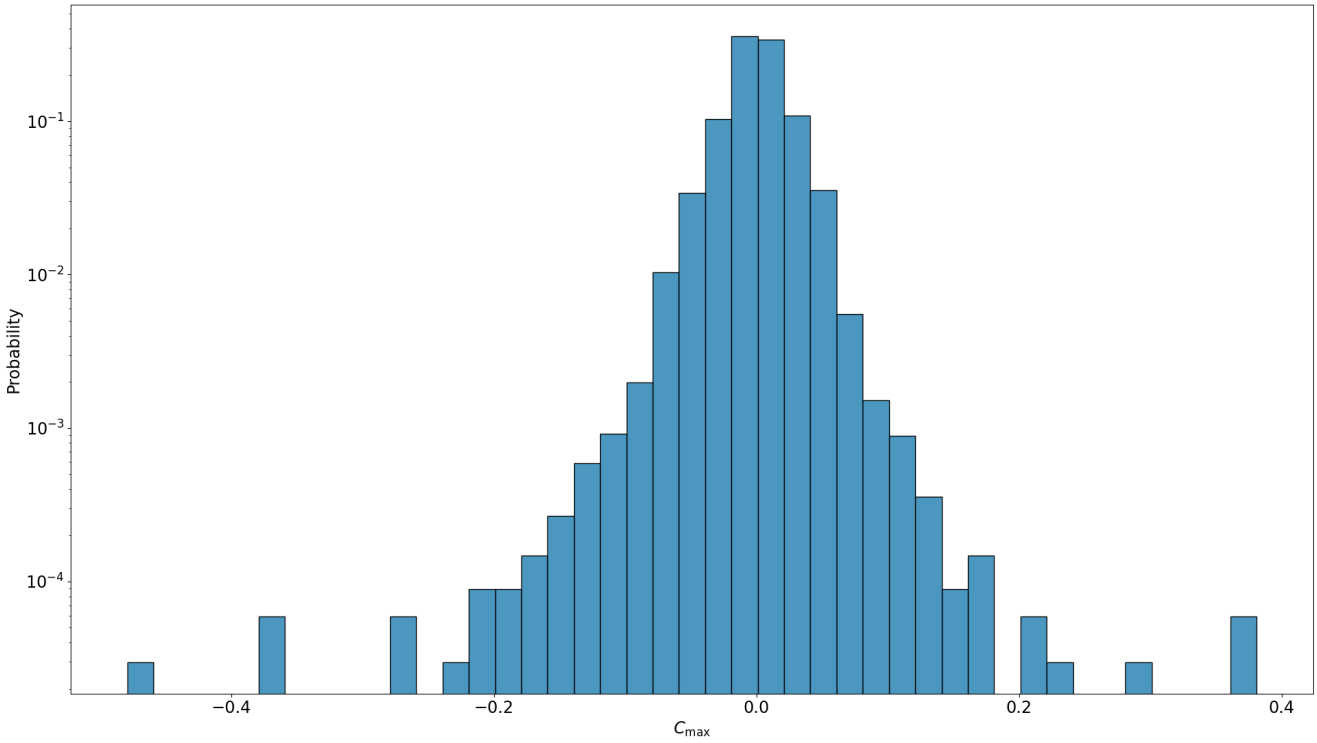

Figure S7. $C_{\max}$ estimation derived from the distribution of bed up-slope angles in flow direction within the magenta box in Fig. S8. The Bedmap2 horizontal grid resolution is 1 km (Fretwell et al., 2013). The bin width is 0.02.

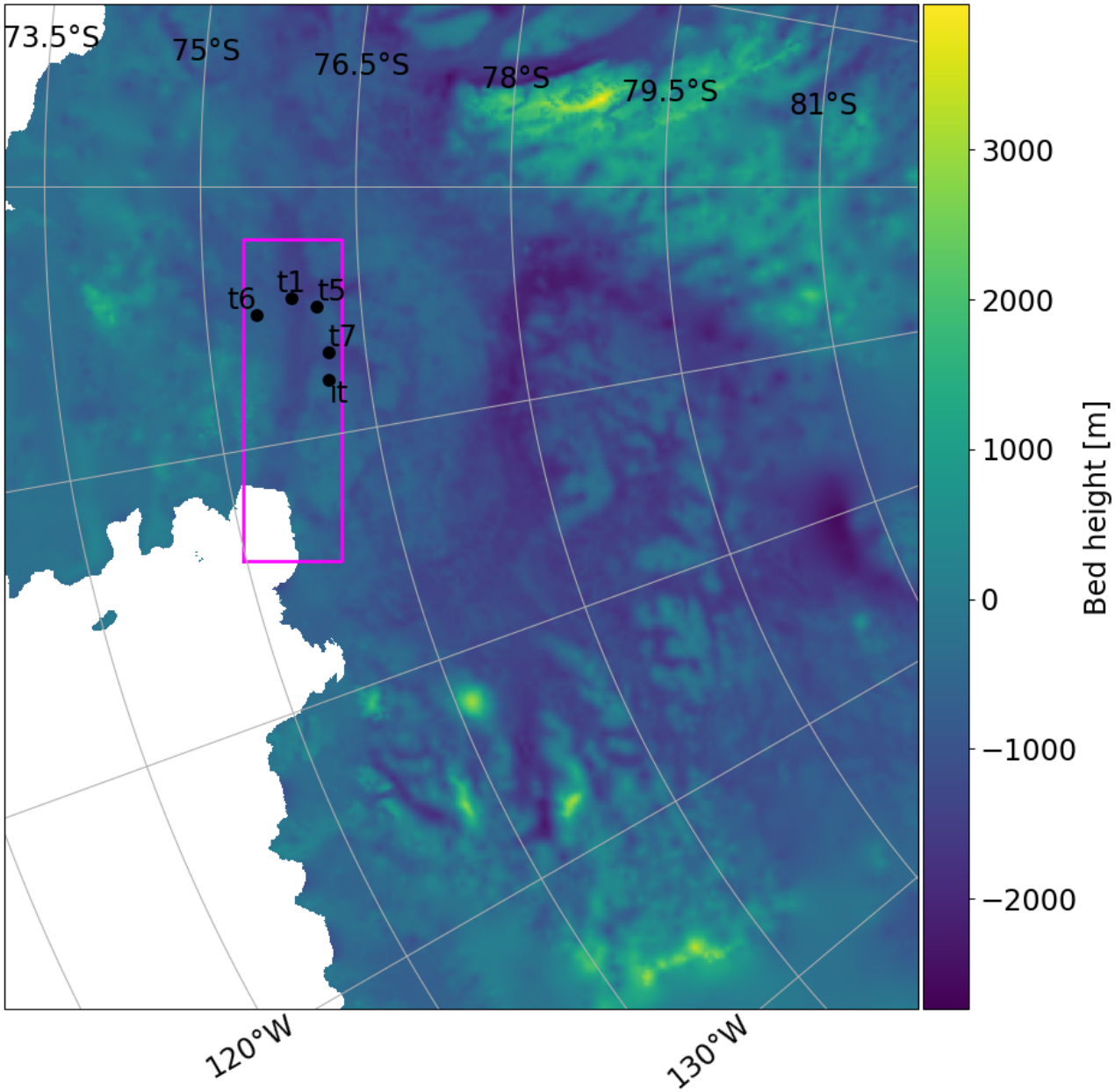

Figure S8. Bed height for areas with ice cover (grounded and floating; based on Bedmap2; Fretwell et al., 2013). The magenta box frames the main trunk of Pine Island Glacier (PIG) and the black dots mark the locations of the acoustic impedance data sites.

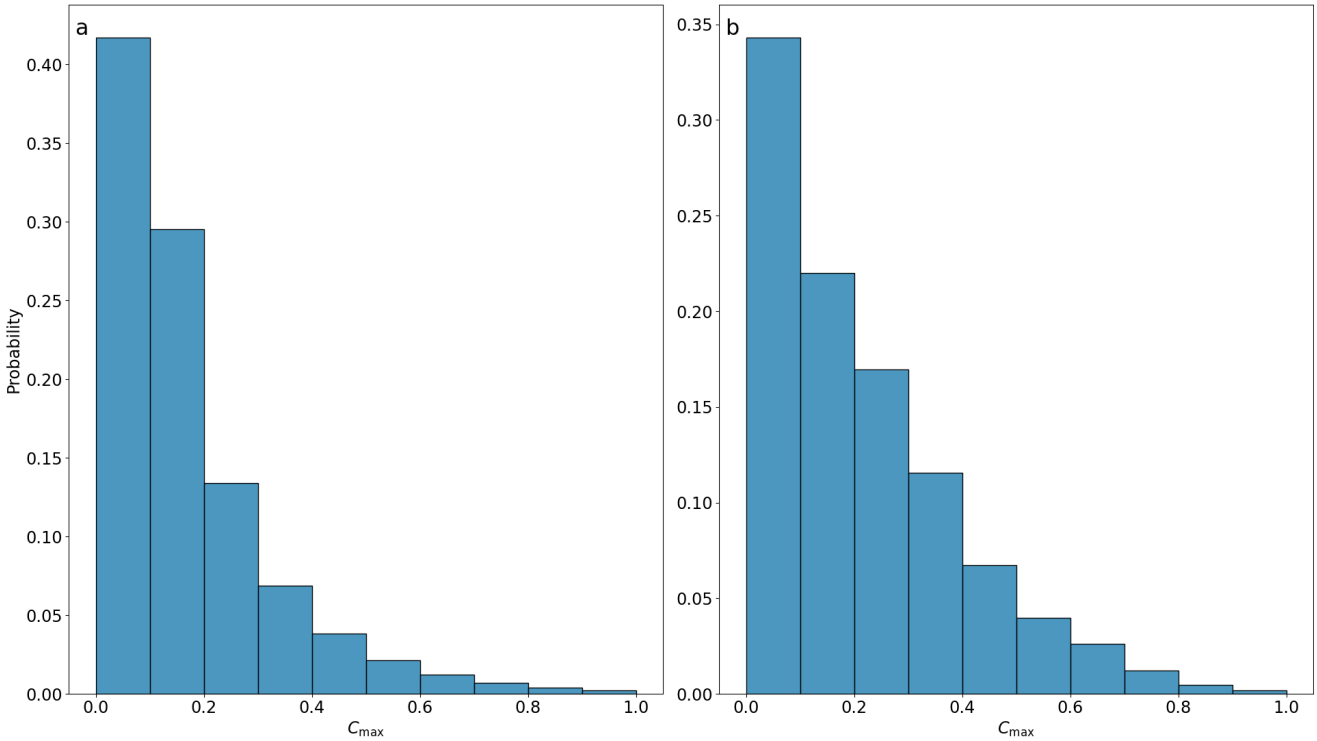

Figure S9. $C_{\max}$ estimation derived from the distribution of bed slope angles from autonomous underwater vehicle (AUV) data collected downstream of Thwaites Glacier (a; 1.5 m horizontal resolution; Graham et al., 2022) and under the Thwaites Eastern Ice Shelf (b; 2 m horizontal resolution; Wåhlin et al., 2026). The bin width is 0.1. $C_{\max}$ values > 1.0 are not shown here. The corresponding spatial distributions are shown in Fig. S10.

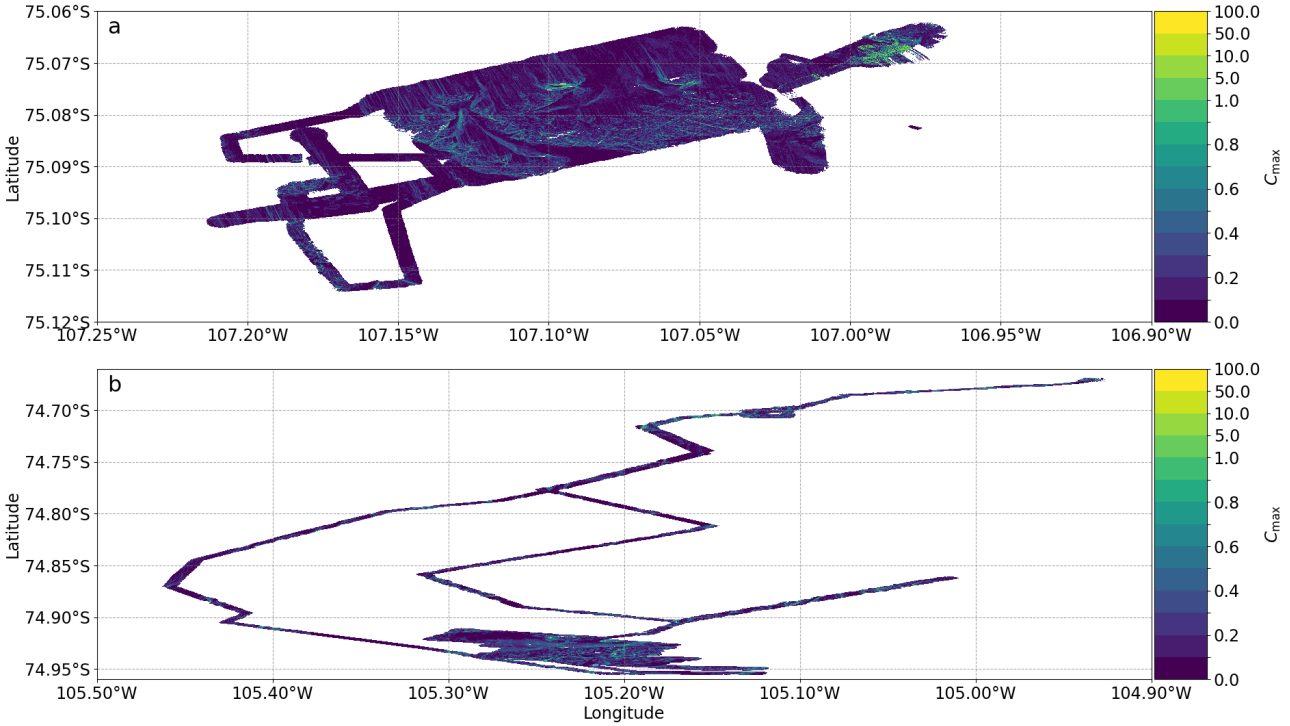

Figure S10. Spatial distribution of the autonomous underwater vehicle (AUV) data shown in Fig. S9 (downstream of Thwaites Glacier in a (Graham et al., 2022); under the Thwaites Eastern Ice Shelf in b (Wåhlin et al., 2026)). Note the change in colorbar step at $C_{\max} = 1.0$.

S7 Acoustic impedance data-model misfit under different sliding laws (maximum 3D)

S7.1 Fixed effective pressure endmember scenarios $N = 0$ Pa and $N = p_\mathrm{i}$

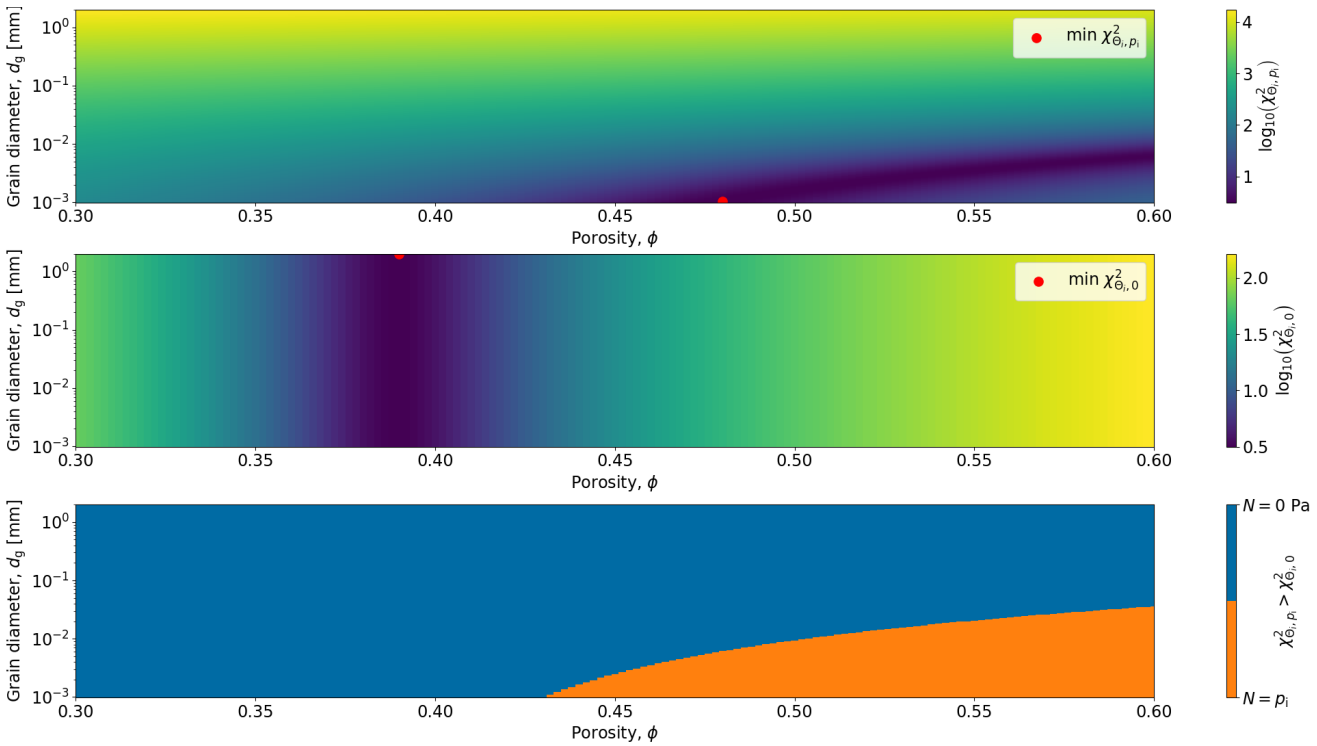

Figure S11. Variations of the misfit $\chi^2_{\Theta_i}$ with the two model parameters grain diameter (d_g) and porosity (ϕ) under the fixed effective pressure endmember scenarios $N = p_\mathrm{i}$ (top panel) and $N = 0$ Pa (center panel). The bottom panel shows the preferred endmember scenario within the parameter space. The red dots mark the minimum misfit.

S7.2 Budd (C_{B})

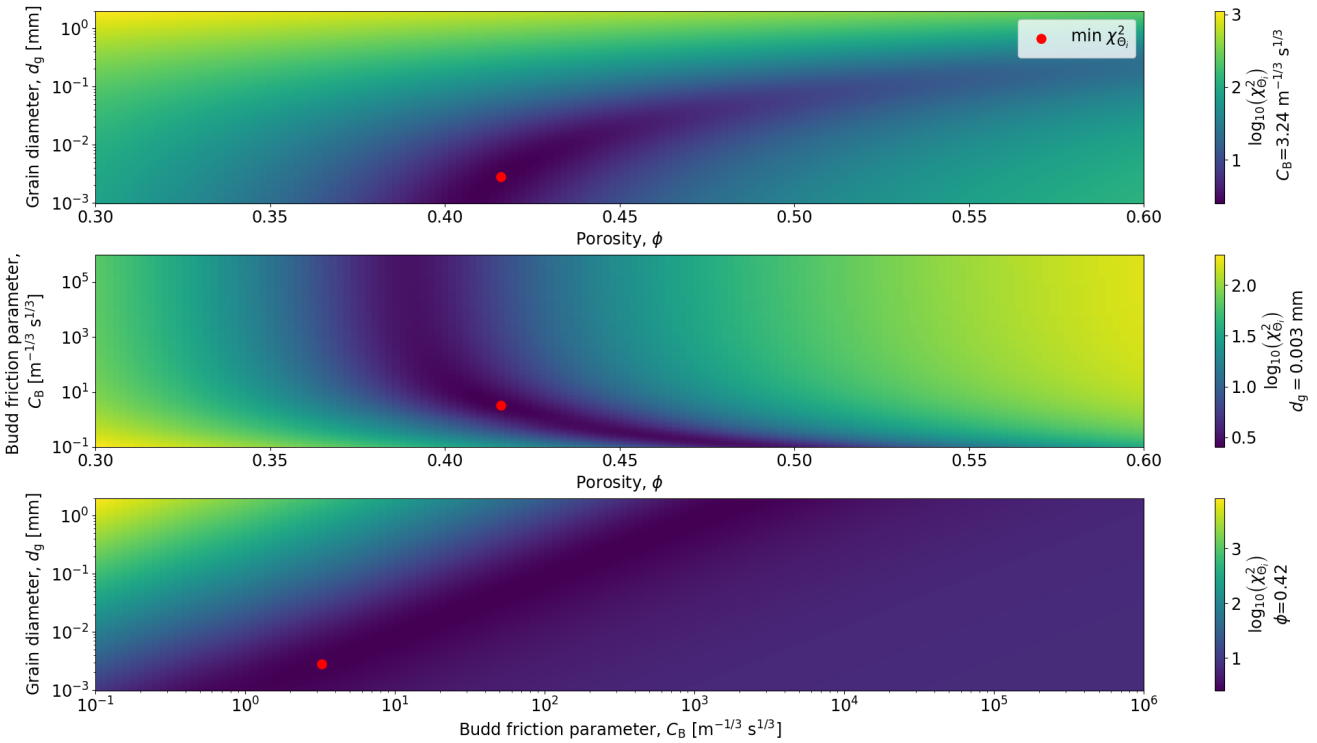

Figure S12. Variations of the misfit $\chi^2_{\Theta_i}$ with the three model parameters grain diameter (d_{g}), porosity (ϕ), and Budd friction parameter (C_{B}) under a Budd sliding law. For the parameter not shown, the value yielding the minimum misfit is used and denoted next to the colorbar of the corresponding panel. The red dots mark the minimum misfit.

S7.3 Tsai-Budd (C_{B})

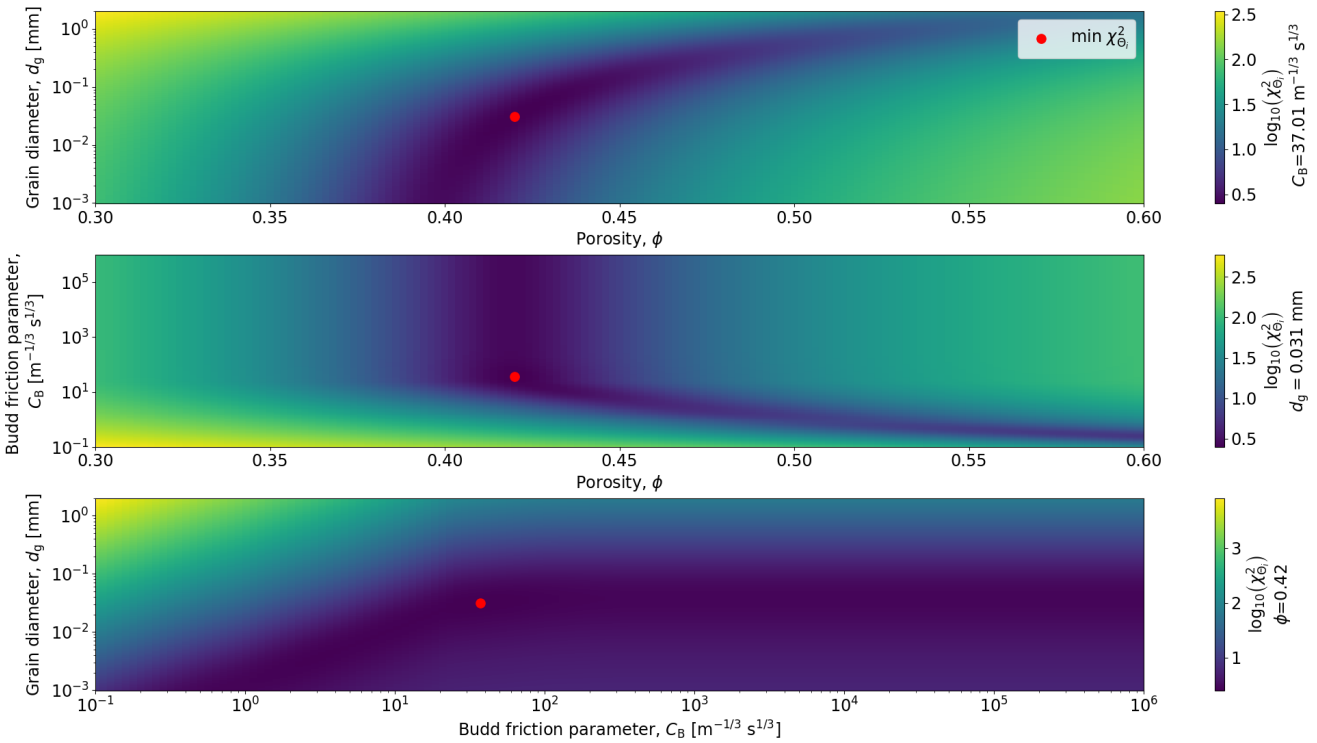

Figure S13. Variations of the misfit $\chi^2_{\Theta_i}$ with the three model parameters grain diameter (d_{g}), porosity (ϕ), and Budd friction parameter (C_{B}) under a Tsai-Budd sliding law (μ fixed at 0.5). Otherwise as Fig. S12.

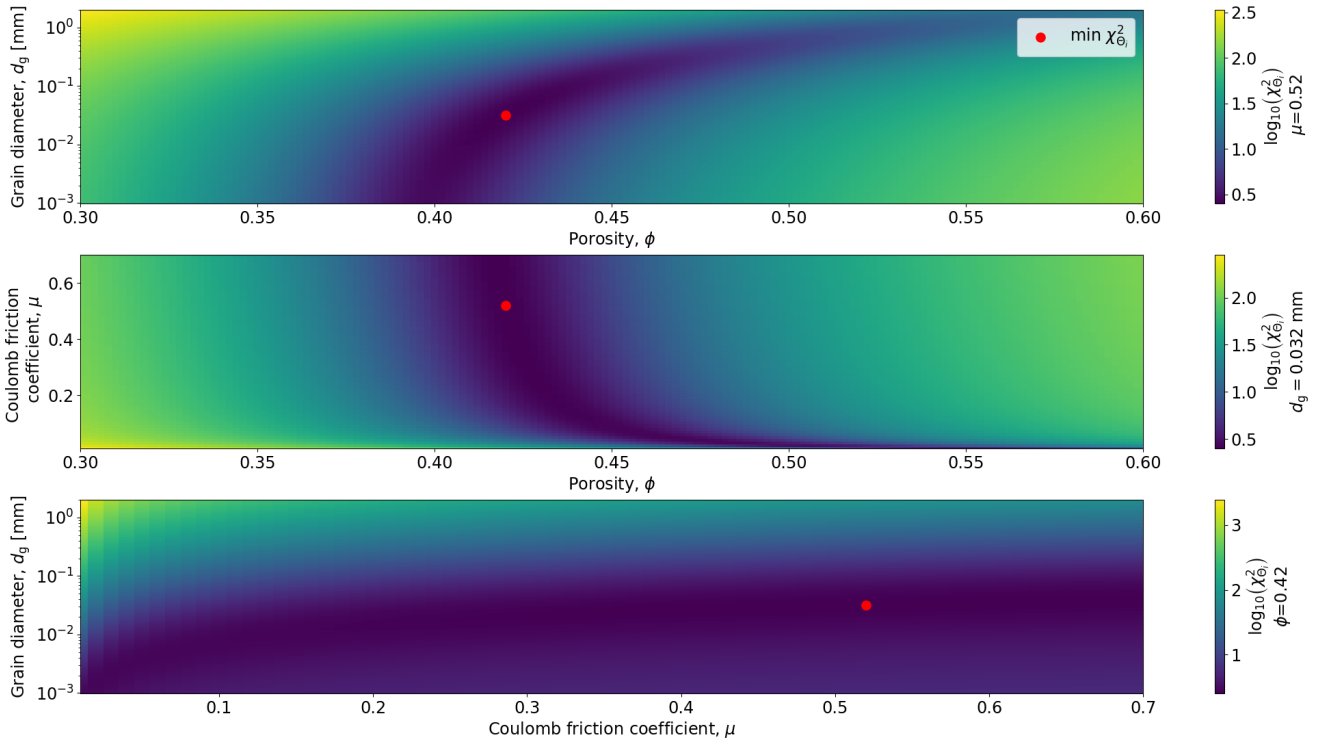

Figure S14. Variations of the misfit $\chi^2_{\Theta_i}$ with the three model parameters grain diameter (d_g), porosity (ϕ), and Coulomb friction coefficient (μ) under a Tsai-Budd sliding law (C_B fixed at 37.01 $m^{-1/3}$ $s^{1/3}$). Otherwise as Fig. S12.

S7.5 Schoof (C_S)

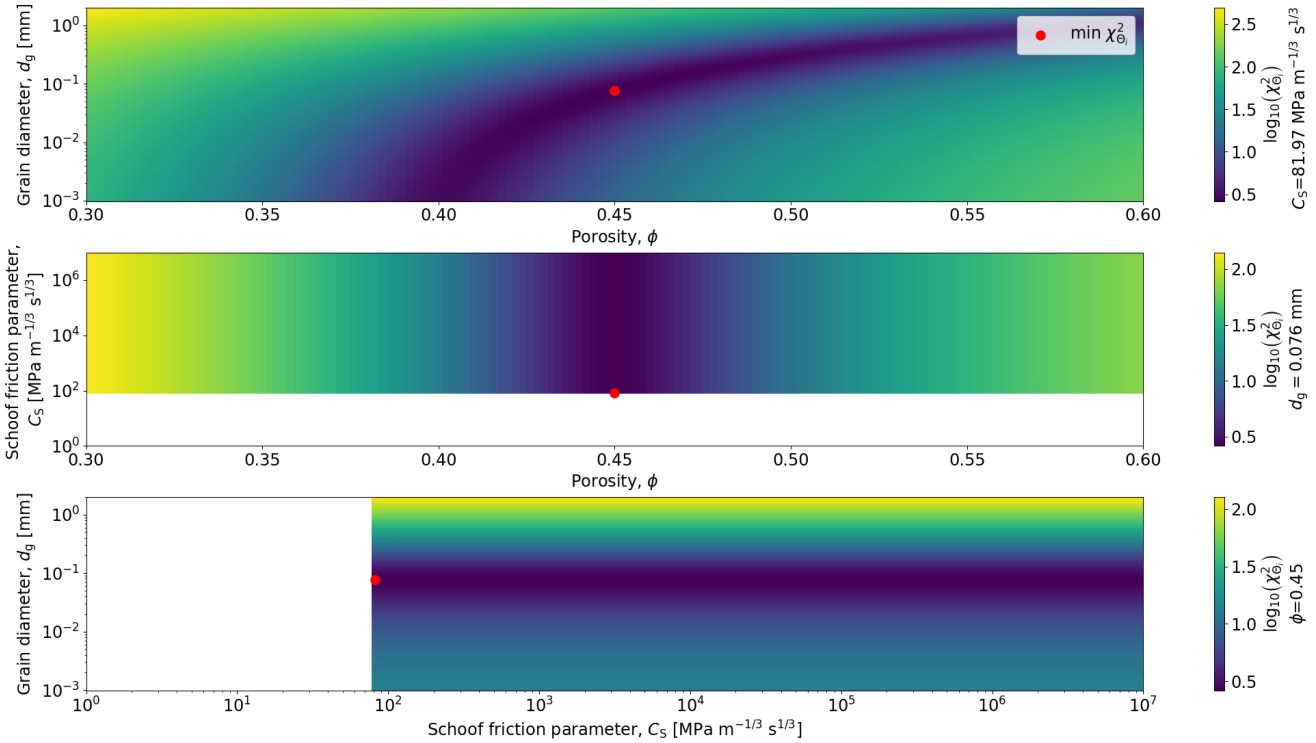

Figure S15. Variations of the misfit $\chi^2_{\Theta_i}$ with the three model parameters grain diameter (d_g), porosity (ϕ), and Schoof friction parameter (C_S) under a Schoof sliding law (C_{max} fixed at 0.2). The determination of $\chi^2_{\Theta_i}$ is only possible when the number of incompatible $u_b - \tau_b$ pairs is small (Sec. S5 and Fig. S16). Otherwise as Fig. S12.

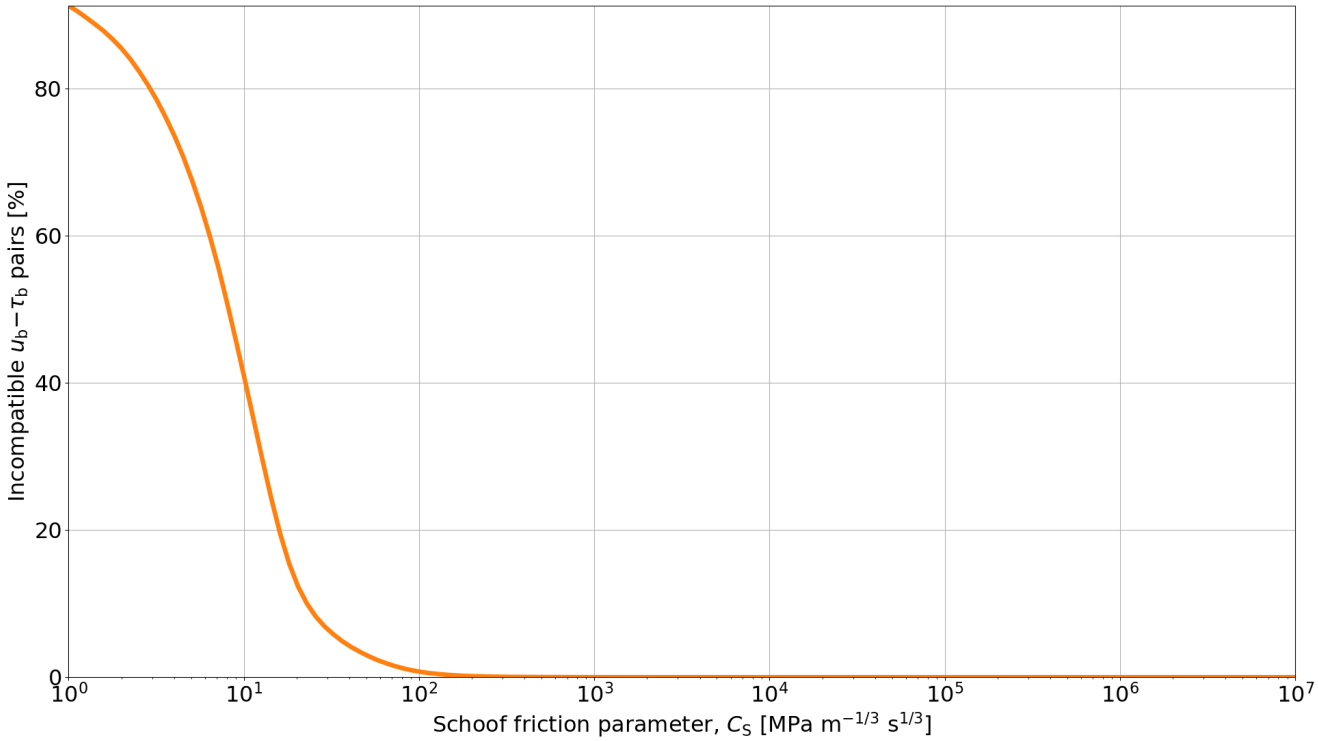

Figure S16. Percentage of incompatible $u_\mathrm{b}-\tau_\mathrm{b}$ pairs under a Schoof sliding law when varying the Schoof friction parameter (C_S; C_max fixed at 0.2).

S7.6 Schoof (C_{max})

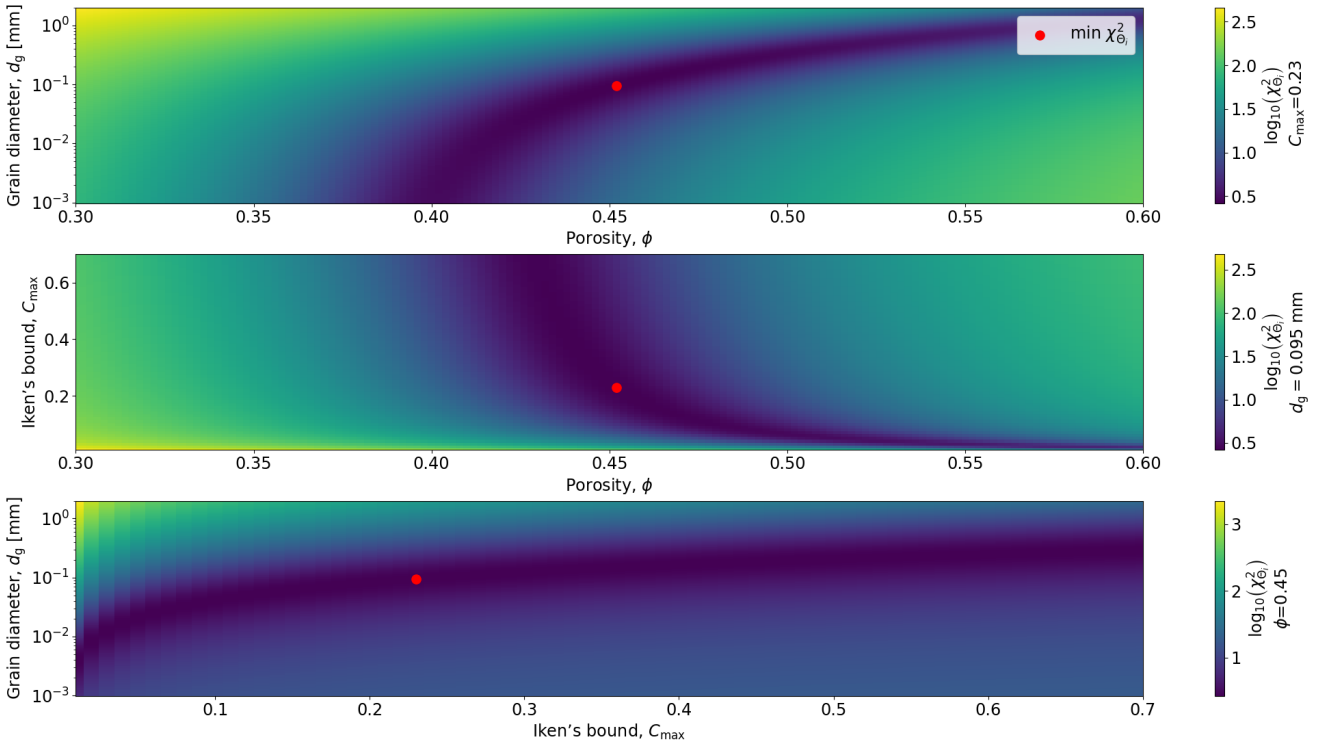

Figure S17. Variations of the misfit $\chi^2_{\Theta_i}$ with the three model parameters grain diameter (d_{g}), porosity (ϕ), and Iken's bound (C_{max}) under a Schoof sliding law (C_{S} fixed at $1 \cdot 10^3$ MPa $\mathrm{m}^{-1/3}$ $\mathrm{s}^{1/3}$; Sec. S5). Otherwise as Fig. S12.

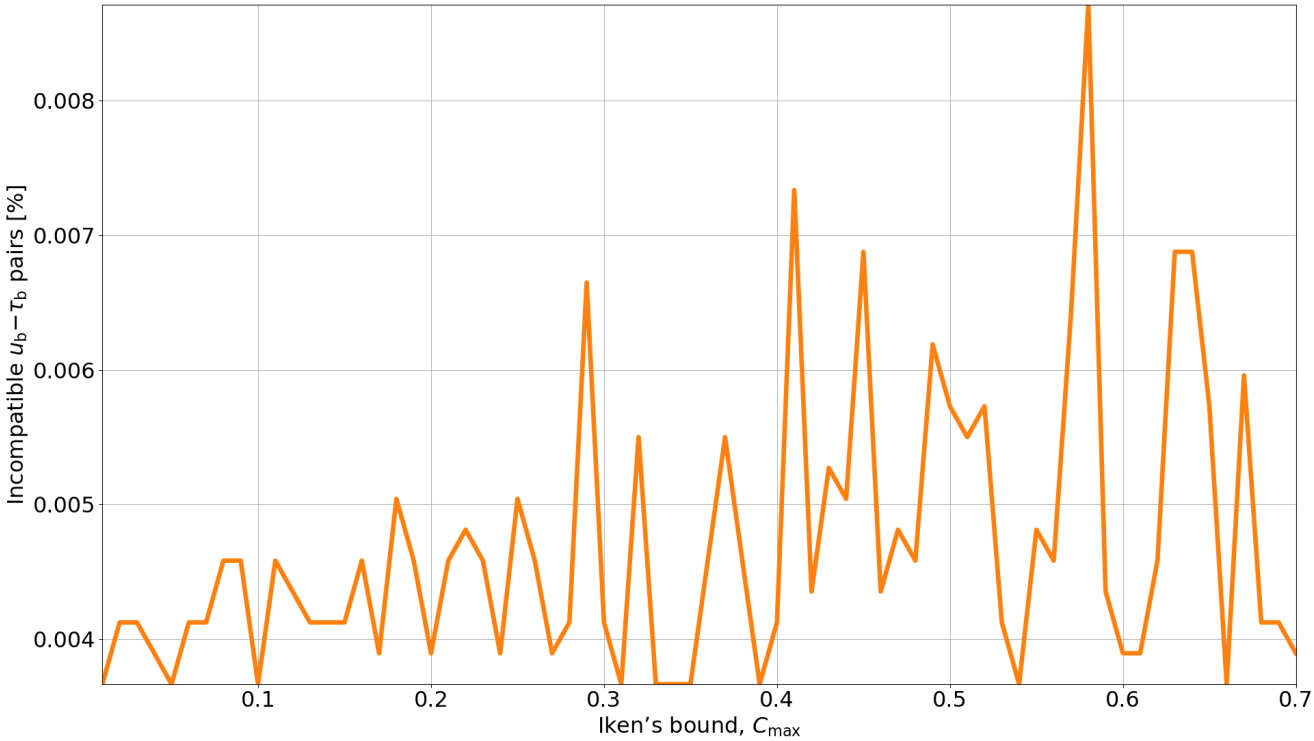

Figure S18. Percentage of incompatible $u_{\mathrm{b}}-\tau_{\mathrm{b}}$ pairs under a Schoof sliding law when varying Iken's bound ($C_{\max}$; C_{S} fixed at $1 \cdot 10^3$ MPa $\mathrm{m}^{-1/3}$ $\mathrm{s}^{1/3}$; Sec. S5).

S7.7 Zoet-Iverson (μ)

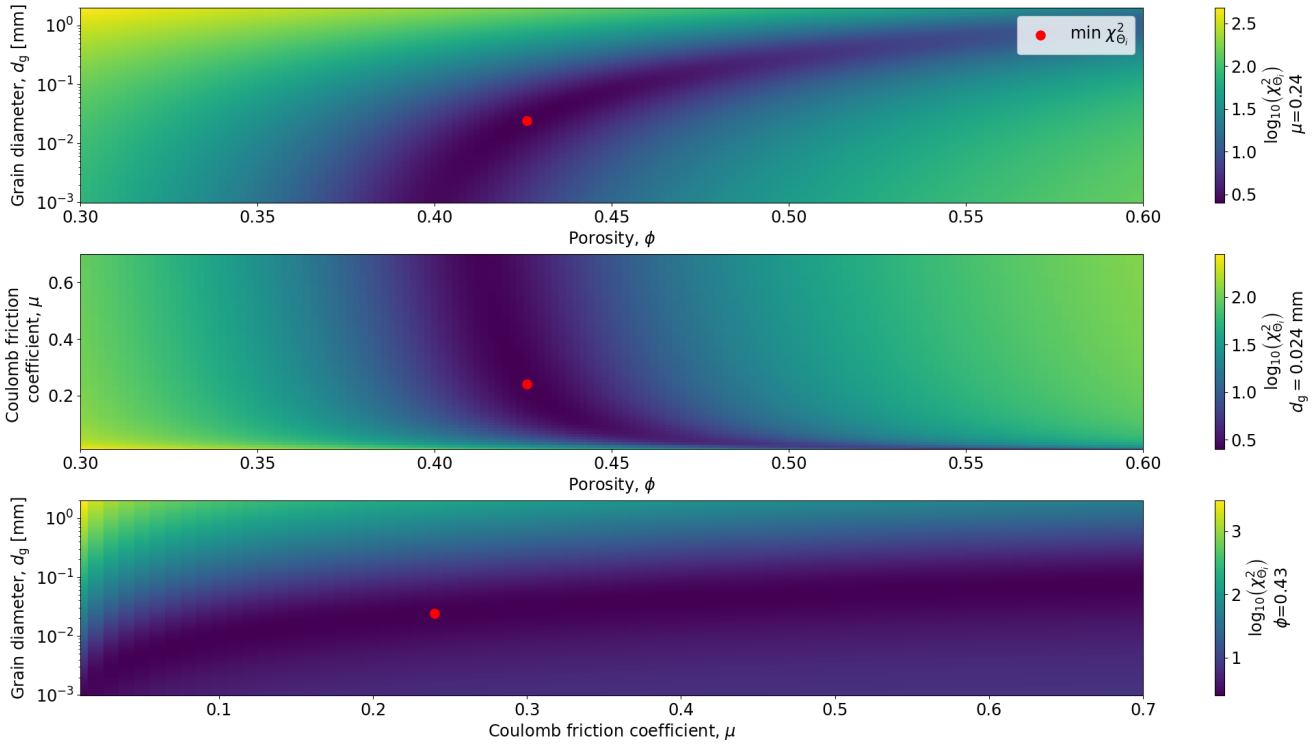

Figure S19. Variations of the misfit $\chi^2_{\Theta_i}$ with the three model parameters grain diameter (d_g), porosity (ϕ), and Coulomb friction coefficient (μ) under a Zoet-Iverson sliding law (C_{ZI} fixed at ~ 340 MPa^{-1} m a^{-1}). Otherwise as Fig. S12.

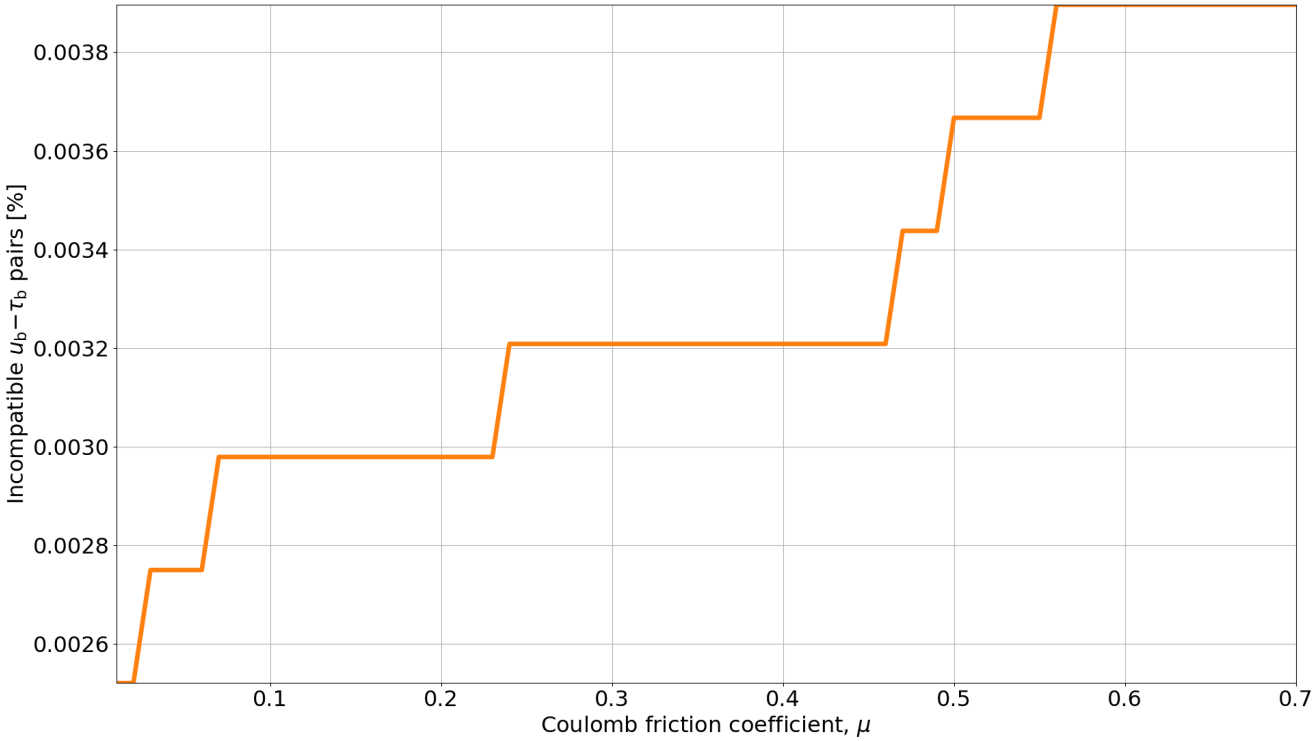

Figure S20. Percentage of incompatible $u_b - \tau_b$ pairs under a Zoet-Iverson sliding law when varying the Coulomb friction coefficient (μ; C_{ZI} fixed at ~ 340 MPa^{-1} m a^{-1}).

S7.8 Zoet-Iverson (C_{ZI})

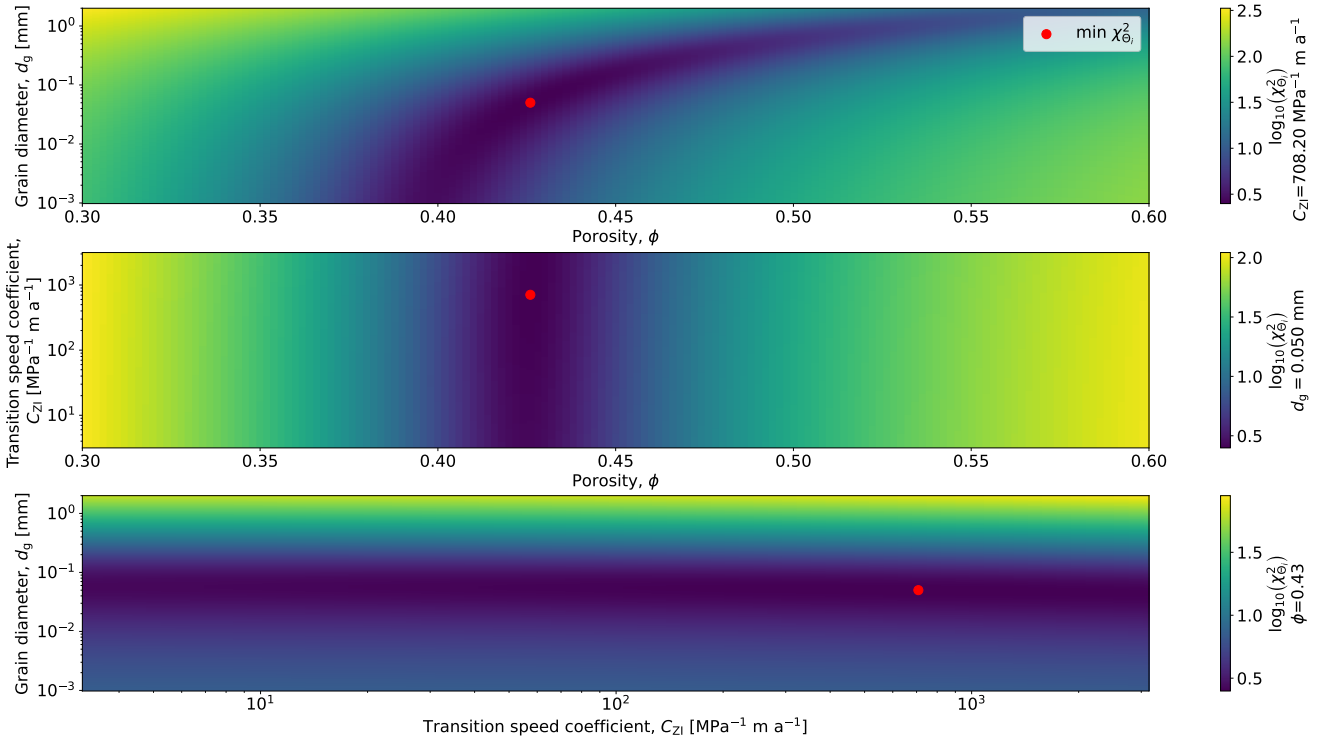

Figure S21. Variations of the misfit $\chi^2_{\Theta_i}$ with the three model parameters grain diameter (d_{g}), porosity (ϕ), and transition speed coefficient (C_{ZI}) under a Zoet-Iverson sliding law (Coulomb friction coefficient μ fixed at 0.5). Otherwise as Fig. S12.

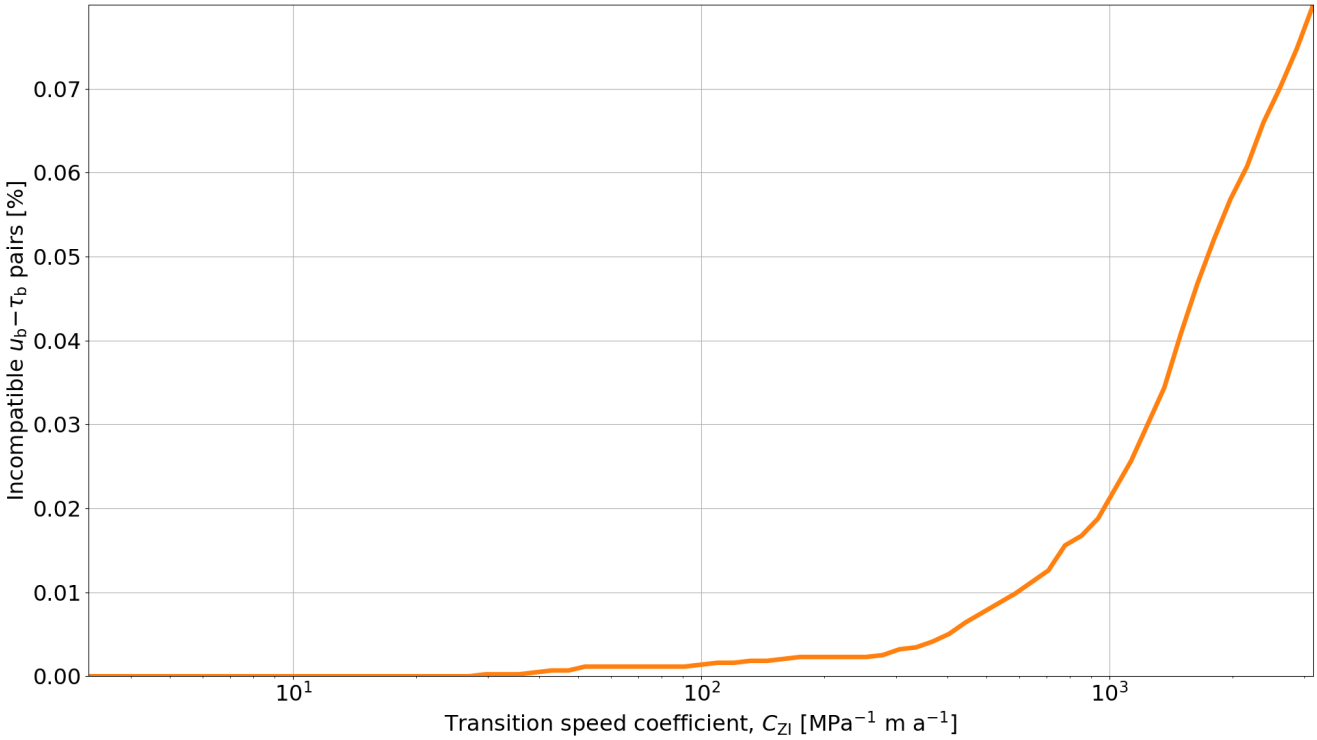

Figure S22. Percentage of incompatible $u_\mathrm{b}-\tau_\mathrm{b}$ pairs under a Zoet-Iverson sliding law when varying the transition speed coefficient (C_ZI; μ fixed at 0.5).

S8 Posterior probabilities when using different fractions of the ice overburden pressure

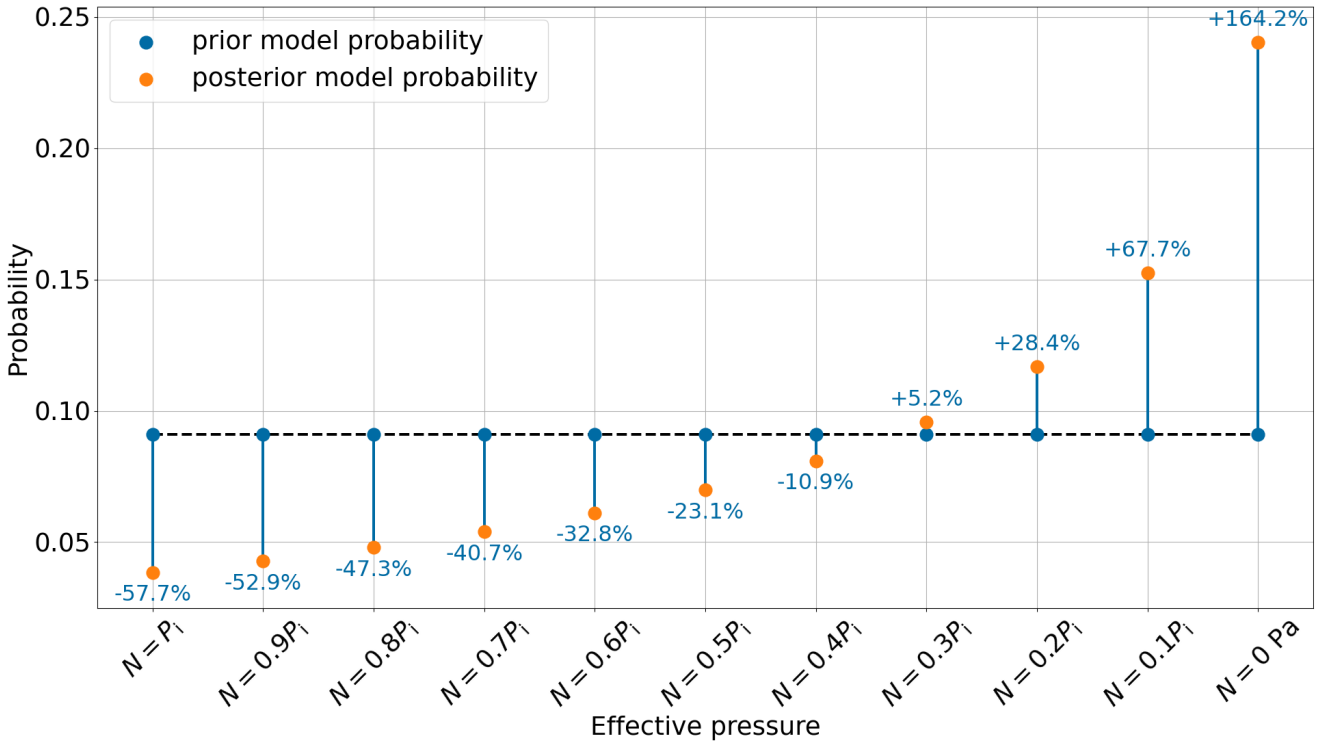

Figure S23. Normalized probabilities (Eq. 20) given the seismic observations collected on PIG when using different fractions of the ice overburden pressure, including the two endmember scenarios ($N = 0$ Pa and $N = p_i$). Otherwise, as Fig. 6 in the main text.

S9 Acoustic impedance for most probable parameters

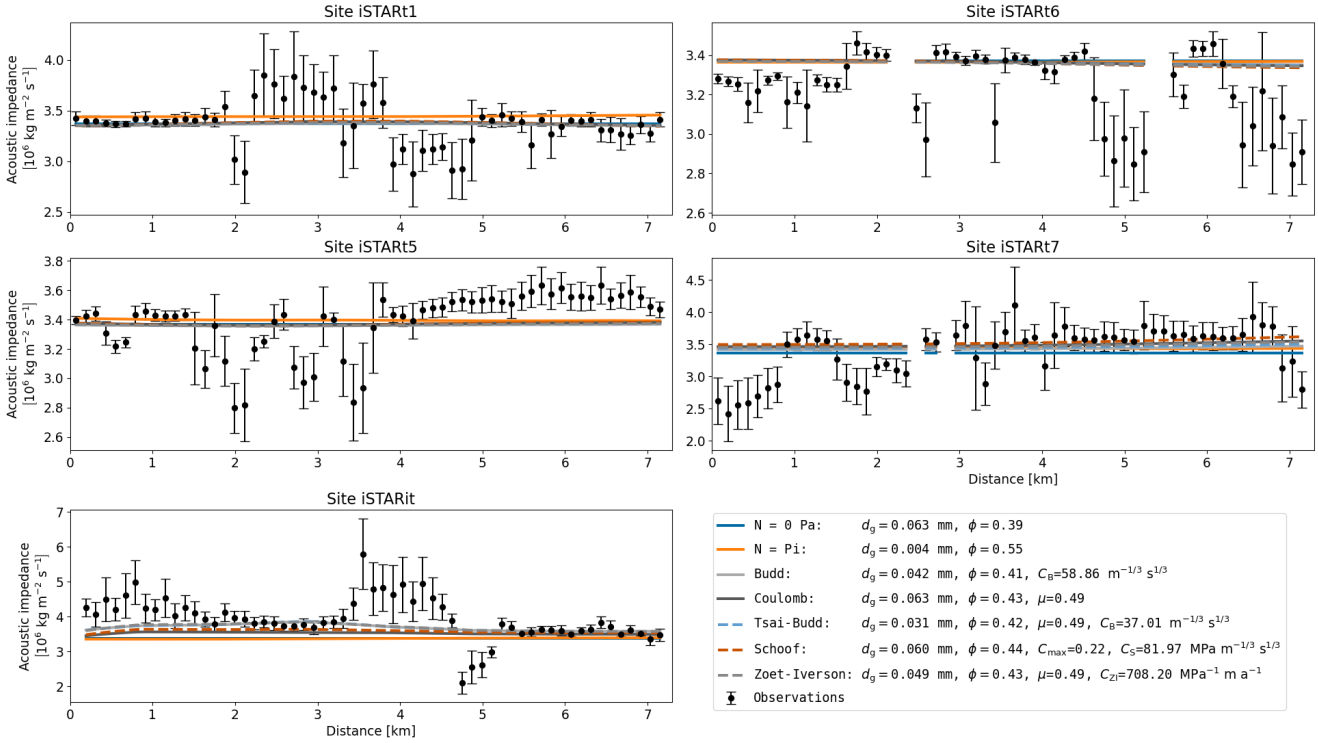

Figure S24. The different panels show the predicted acoustic impedance at the five data sites. For all sliding laws, the acoustic impedance curve is based on the MAP (highest posterior probability) model parameters shown in the legend.

S10 Posterior probabilities for (log-)uniform prior distributions

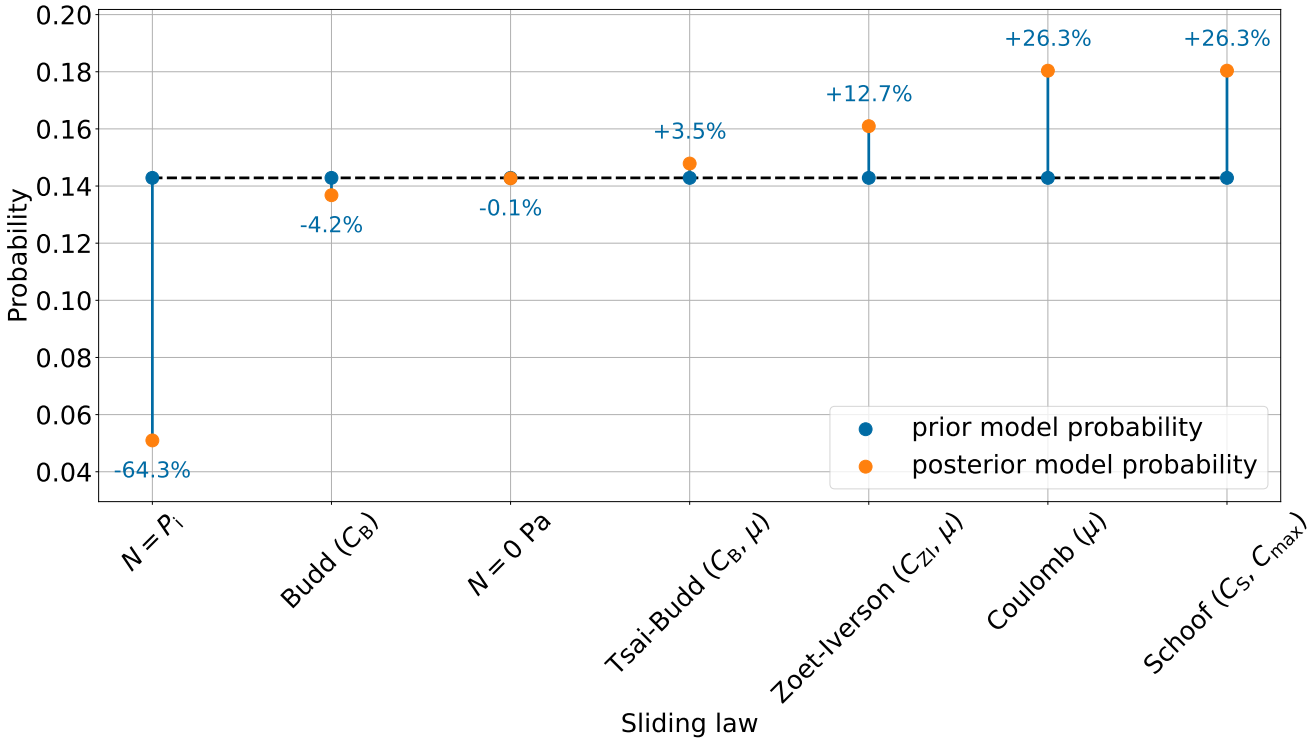

Figure S25. Normalized probabilities (Eq. 20) of all sliding laws examined in this study given the acoustic impedance observations collected on PIG, and log-uniform prior distributions for scaling coefficients and uniform priors for other parameters. Otherwise, as Fig. 6 in the main text.

S11 Effective pressure for most probable parameters

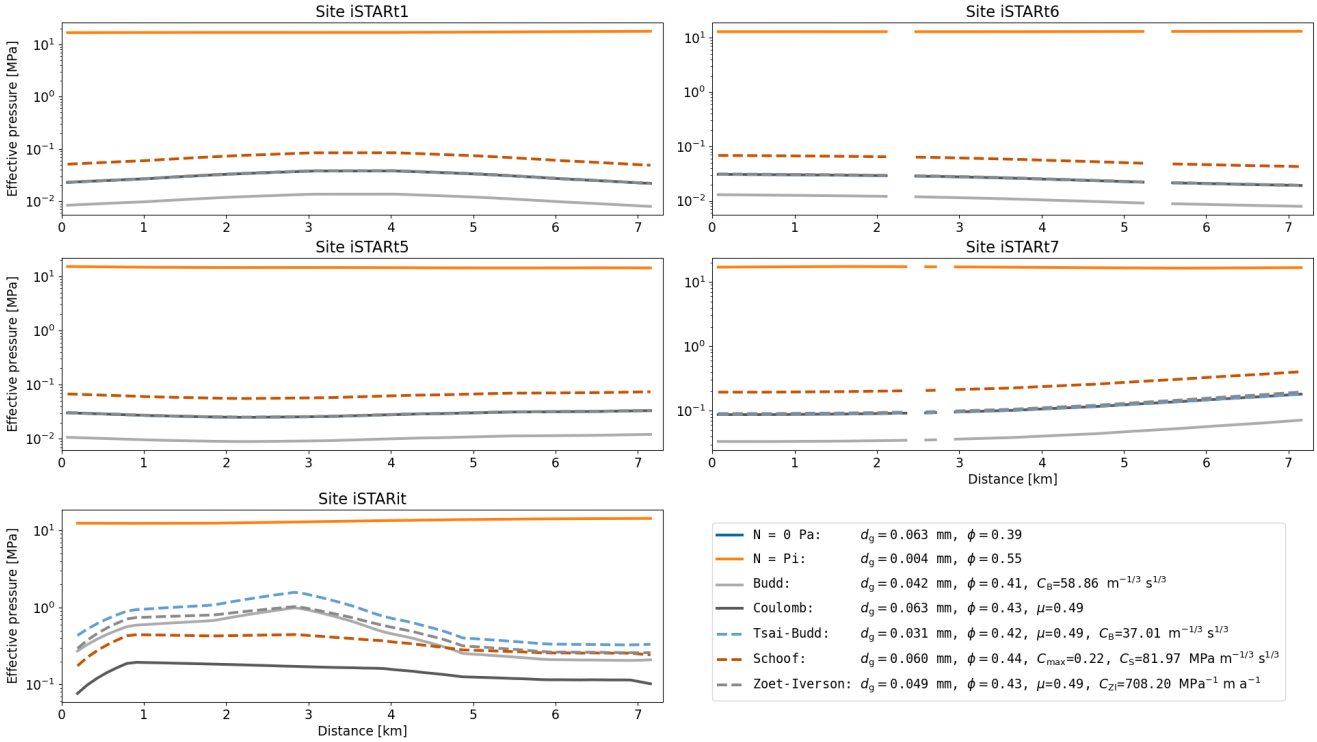

Figure S26. The different panels show the predicted effective pressure at the five data sites. For all sliding laws, the effective pressure curve is based on the MAP (highest posterior probability) model parameters. By definition, the low effective pressure endmember scenario has $N = 0$ Pa and only the MAP parameter values are shown here (not the curve itself). Note the logarithmic scale of the y-axes.

References

Brondex, J., Gagliardini, O., Gillet-Chaulet, F., and Durand, G.: Sensitivity of grounding line dynamics to the choice of the friction law, Journal of Glaciology, 63, 854–866, https://doi.org/10.1017/jog.2017.51, 2017.

Brondex, J., Gillet-Chaulet, F., and Gagliardini, O.: Sensitivity of centennial mass loss projections of the Amundsen basin to the friction law, The Cryosphere, 13, 177–195, https://doi.org/10.5194/tc-13-177-2019, 2019.

Fretwell, P., Pritchard, H. D., Vaughan, D. G., Bamber, J. L., Barrand, N. E., Bell, R., Bianchi, C., Bingham, R. G., Blankenship, D. D., Casassa, G., Catania, G., Callens, D., Conway, H., Cook, A. J., Corr, H. F., Damaske, D., Damm, V., Ferraccioli, F., Forsberg, R., Fujita, S., Gim, Y., Gogineni, P., Griggs, J. A., Hindmarsh, R. C., Holmlund, P., Holt, J. W., Jacobel, R. W., Jenkins, A., Jokat, W., Jordan, T., King, E. C., Kohler, J., Krabill, W., Riger-Kusk, M., Langley, K. A., Leitchenkov, G., Leuschen, C., Luyendyk, B. P., Matsuoka, K., Mouginot, J., Nitsche, F. O., Nogi, Y., Nost, O. A., Popov, S. V., Rignot, E., Rippin, D. M., Rivera, A., Roberts, J., Ross, N., Siegert, M. J., Smith, A. M., Steinhage, D., Studinger, M., Sun, B., Tinto, B. K., Welch, B. C., Wilson, D., Young, D. A., Xiangbin, C., and Zirizzotti, A.: Bedmap2: Improved ice bed, surface and thickness datasets for Antarctica, Cryosphere, 7, 375–393, https://doi.org/10.5194/tc-7-375-2013, 2013.

Graham, A. G., Wåhlin, A., Hogan, K. A., Nitsche, F. O., Heywood, K. J., Totten, R. L., Smith, J. A., Hillenbrand, C. D., Simkins, L. M., Anderson, J. B., Wellner, J. S., and Larter, R. D.: Rapid retreat of Thwaites Glacier in the pre-satellite era, Nature Geoscience, 15, 706–713, https://doi.org/10.1038/s41561-022-01019-9, 2022.

Smith, J. A., Hillenbrand, C.-D., Kuhn, G., Larter, R. D., Graham, A. G., Ehrmann, W., Moreton, S. G., and Forwick, M.: Deglacial history of the West Antarctic Ice Sheet in the western Amundsen Sea Embayment, Quaternary Science Reviews, 30, 488–505, https://doi.org/https://doi.org/10.1016/j.quascirev.2010.11.020, 2011.

Smith, J. A., Andersen, T. J., Shortt, M., Gaffney, A. M., Truffer, M., Stanton, T. P., Bindschadler, R., Dutrieux, P., Jenkins, A., Hillenbrand, C. D., Ehrmann, W., Corr, H. F., Farley, N., Crowhurst, S., and Vaughan, D. G.: Sub-ice-shelf sediments record history of twentieth-century retreat of Pine Island Glacier, Nature, 541, 77–80, https://doi.org/10.1038/nature20136, 2017.

Wåhlin, A., Stedt, F., Wahlgren, S., Yuan, X., Billman, M., and Lee, W. S.: Raw data from Ran AUV missions ANA14B_01, ANA14B_02 and ANA14B_03 performed during the ANA14B RVIB Araon expedition to the Amundsen Sea, https://doi.org/10.5878/ns3m-fs31, 2026.

Zoet, L. K. and Iverson, N. R.: A slip law for glaciers on deformable beds, Science, 368, 76–78, https://doi.org/10.1126/science.aaz1183, 2020.